Dirac Hierarchy in Acoustic Topological Insulators

Li-Yang Zheng[*] and Johan Christensen[†]

Department of Physics, Universidad Carlos III de Madrid, ES-28916 Leganès, Madrid, Spain

Dirac cones are essential features of the electronic band structure of materials like graphene and topological insulators (TIs). Lately, this avenue has found a growing interest in classical wave physics by using engineered artificial lattices. Here, we demonstrate an acoustic 3D honeycomb lattice that features a Dirac hierarchy comprising an eightfold bulk Dirac cone, a 2D fourfold surface state Dirac cone, and a 1D twofold hinge state Dirac cone. The lifting of the Dirac degeneracy in each hierarchy authorizes the 3D lattice to appear as a first-order TI with 2D topological surface states, a second-order TI exhibiting 1D hinge states, and a third-order TI of 0D midgap corner states. Analytically we discuss the topological origin of the surface, hinge, and corner states, which are all characterized by out-of-plane and in-plane winding numbers. Our study offers new routes to control sound and vibration for acoustic steering and guiding, on-chip ultrasonic energy concentration, and filtering to name a few.

Topological insulators and phases pertain to a prominent key frontier in condensed matter physics that has provided many exotic directions to inspire contemporary wave control. Topological materials and their electronic band structure belong to a different topological class compared to ordinary insulators and metals [1–4]. Their topological phases describe global properties of quantum states in materials, which are resilient against perturbations that preserve certain symmetries, such as inversion, rotation, chirality, etc. Exotic quantum states have been investigated extensively in various nanostructures such as high-quality crystals, thin films, and epitaxially grown structures. Many topological crystalline insulators have been engineered into nanostructures through mechanical exfoliation or direct growth synthesis [5–7]. Recently, a catalog was introduced containing several thousands topological materials, which were gathered using only symmetry data [8].

On a macro level where engineered acoustic and mechanical structures are investigated, the fabrication is much easier and so is the experimental characterization. The field of topological phononics has borrowed a number of blueprints used in electronic materials. However, when constructed for classical waves, the sonic crystals and metamaterials are chiefly based on manufactured scatterers and resonance elements typically drilled or carved in metals or 3D printed [9]. Hence, it is straightforward to craft topological phases in acoustic lattices at desired spectral regimes, by appropriately designing the building blocks [10]. The hallmark of topological insulators (TIs) is wave propagation and guiding in the absence of backscattering by means of exotic surface and edge-state excitation. Colorful examples comprise acoustic topological edge states, which have been implemented in time-reversal broken structures to mimic the quantum Hall effect.

Further, pseudospins have been designed to emulate the quantum spin-Hall (QSH) effect, and quantum valley-Hall phases have been engineered through the breaking of the mirror symmetry [11–25]. As a counterpart to topological systems abiding by the conventional bulk-edge correspondence, 0D corner states in 2D and 3D have been successfully demonstrated in very complex higher-order topological insulators (HOTIs) [26–31]. In this Letter, we present an approach which rests on stacking multiple 2D honeycomb monolayers of interconnected waveguide channels, in order to establish a Dirac hierarchy across multiple dimensions. Since it is still very challenging to construct 3D HOTIs as existing means require either highly cumbersome coupling strengths or extremely complicated geometrical structures [32–35], our strategy enables the creation of sonic multifold Dirac cones (DCs) in the bulk, at the surface and hinges with associated hierarchical phase transitions using the same 3D base configuration.

We begin with an extended honeycomb cell containing six sublattices in which the intermolecular coupling α equals the intramolecular one β [Fig. 1(a)]. This design ensures a double Dirac cone (DDC) (fourfold degeneracy) at the Brillouin zone (BZ) center thanks to band folding of DCs from the K/K' points. Subsequently, we introduce chiral symmetry along the perpendicular direction (z axis) to the honeycomb plane (xy plane) by stacking several monolayers of alternating interlayer coupling strengths γ and γ', in order to form a layered Su-Schrieffer-Heeger (SSH) chain [Fig. 1(a) (bottom)]. Because of the chiral symmetry, the eigenstates of the system come in pairs, i.e., each bulk state at energy $+\Delta$ has a chiral partner at $-\Delta$. When $\gamma = \gamma'$, the DDC pair of two sublayers degenerates at $\Delta = 0$, leading to an eightfold DC at the Z point as shown in Fig. 1(a) (top), which can also be interpreted as the
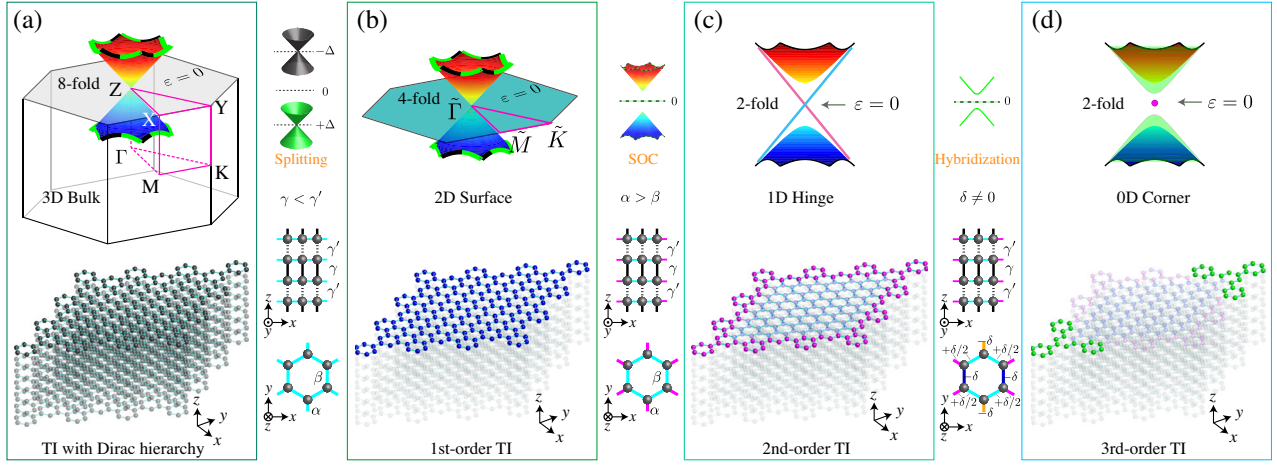
FIG. 1. Acoustic Dirac hierarchy. (a) 3D honeycomb lattice made of multiple stacked Kekulé monolayers. An eightfold Dirac cone (DC) appears at energy $\varepsilon = 0$ at the Z point of the Brillouin zone (BZ). (b) The eightfold degeneracy becomes a first-order TI after splitting into two fourfold DCs when the interlayer coupling $\gamma < \gamma'$. (c) A second-order TI with a pair of helical hinge states (magenta and cyan lines) is unwrapped when SOC is induced via appropriate intralayer coupling, i.e., $\alpha > \beta$. (d) Last, the 3D lattice transitions into a third-order TI with a pair of midgap corner states (magenta dots) through mirror breaking by adding vertical coupling $-\delta$ to the bonds along the y axis, and $+\delta/2$ to the remaining ones.

consequence of band folding the in-plane DDC along the z direction. From here on, the Dirac hierarchy is born in the bulk and cunningly unwrapped at the surface, hinges, and corners. Thus, applying alternating interlayer coupling $\gamma/\gamma' < 1$ splits the eightfold DC with a first-order topological band gap that contains a fourfold surface DC, see Fig. 1(b) (top). If we further enforce a Kekulé distortion $\alpha > \beta$ to the extended cell, the surface DDC is gapped, i.e., the 3D structure becomes a second-order TI, supporting a pair of gapless hinge states (twofold hinge DC) [Fig. 1(c)]. Also, the twofold hinge DC can be gapped by breaking the mirror symmetry ($\delta \neq 0$) as shown in Fig. 1(d). Therefore, the last nested element appears in the form of midgap corner states of the third-order TI [magenta, see Fig. 1(d)], which all together shows how the Dirac hierarchy elegantly enables the targeting of exotic topological states at various dimensions by deterministic interlayer and intralayer engineering.

The Dirac hierarchy, using a Kekulé-layered SSH chain, allows us to classify the system through a decoupling of the master Hamiltonian,

$$\mathcal{H} = \mathcal{H}_z \otimes I_6 + I_2 \otimes \mathcal{H}_{xy}, \qquad (1)$$

where $\mathcal{H}_z = \gamma'_0 \mathbf{g}(q_z)\boldsymbol{\sigma}$ is the SSH Hamiltonian with $\mathbf{g}(q_z) = (g_x, g_y) = (\gamma/\gamma' + \cos q_z, -\sin q_z)$ and $\boldsymbol{\sigma}$ the Pauli matrix. $\chi_0 = \chi/t$ ($\chi = \alpha, \beta, \gamma, \gamma'$) is the normalized coupling with $t = \alpha + 2\beta + \gamma + \gamma'$. $\mathcal{H}_{xy} = [0, \mathbf{h}(q_x, q_y); \mathbf{h}^*(q_x, q_y), 0]$ is the Kekulé Hamiltonian with $\mathbf{h}(q_x, q_y)$ a 3×3 matrix, see Supplemental Material [36]. q_x, q_y, and q_z are the normalized wave vectors along the x, y, and z directions, respectively. I_N is a $N \times N$ identity matrix. Note that $\mathcal{H}_z$ ($\mathcal{H}_{xy}$) has chiral symmetry Γ_j ($\Gamma_j^2 = 1$) satisfying

$\Gamma_j \mathcal{H}_j \Gamma_j = -\mathcal{H}_j$ ($j = z, xy$), see Supplemental Material [36]. The eigenenergy of the system is given by

$$\varepsilon = \varepsilon_z + \varepsilon_{xy} \qquad (2)$$

and expresses that it is composed of two independent parts: the out-of-plane SSH eigenenergy ε_z and the in-plane Kekulé eigenenergy ε_{xy}. The complete set of eigenstates of $\mathcal{H}$ can be expressed as $\boldsymbol{\psi} = \boldsymbol{\phi}_z \otimes \boldsymbol{\phi}_{xy}$, where $\boldsymbol{\phi}_z$ ($\boldsymbol{\phi}_{xy}$) denotes the eigenstate of $\mathcal{H}_z$ ($\mathcal{H}_{xy}$). From this notation we gather: if $\boldsymbol{\phi}_z$ and $\boldsymbol{\phi}_{xy}$ are bulk states, $\boldsymbol{\psi}$ is a bulk state too. If $\boldsymbol{\phi}_z$ is an edge state and $\boldsymbol{\phi}_{xy}$ is a bulk state, $\boldsymbol{\psi}$ is a surface state. Last, if $\boldsymbol{\phi}_z$ is an edge state and $\boldsymbol{\phi}_{xy}$ is an edge (or 2D corner) state, $\boldsymbol{\psi}$ is a hinge (or 3D corner) state.

Based on Eq. (2), the dispersion relation of the 3D crystal comprising twelve bands when $\alpha = \beta = 0.09$ and $\gamma = \gamma' = 0.365$ is shown in Fig. 2(a), see the schematic in Supplemental Material [36]. Because of the chiral symmetry Γ_z, the bulk state at $+\Delta + \varepsilon_{xy}$ has a chiral partner at $-\Delta + \varepsilon_{xy}$. Also, the chiral symmetry Γ_{xy} further constrains the bulk bands to be symmetrical with respect to zero energy. Since $\varepsilon_z = 0$ when $q_z = \pi$, the six bands given by ε_{xy} degenerate with their chiral partners. Interestingly, at the Z point, a DDC degenerates with its chiral partner to form an eightfold DC, whereas the remaining two chiral pairs are symmetrically offset from zero energy. The eigenfields of the eightfold degeneracy at the Z point [inset of Fig. 2(a)] underline the dipole $\mathbf{p}$ and quadrupole $\mathbf{d}$ nature in addition to either symmetric or asymmetric mode profiles. By introducing a contrast among the interlayer couplings, e.g., $\gamma = 0.09$ and $\gamma' = 0.64$, the eightfold degeneracy is split symmetrically into a DDC pair as shown in Fig. 2(b).
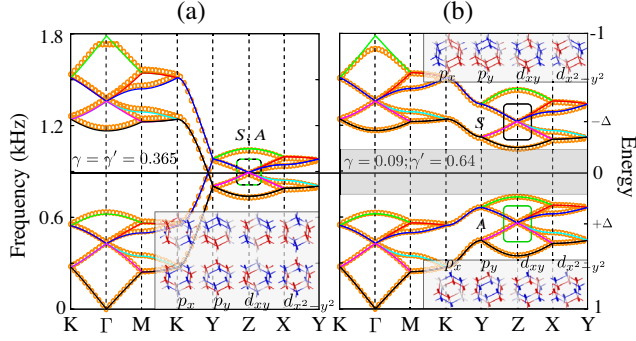
FIG. 2. Bands and eigenfields of the degenerate and split DCs. (a) The eightfold degeneracy at the Z point comprises overlapping symmetric (S) and asymmetric (A) DDCs. The colored lines represent the six theoretically obtained chiral bands. The circles mark the numerical results. Inset: the eigenfields of the Dirac point with dipole p and quadrupole d nature. (b) Splitting of the symmetric and asymmetry DDCs for interlayer coupling strengths, $\gamma < \gamma'$. Insets: the eigenfields of the S- and A-type DDCs.

Their corresponding eigenfields [insets of Fig. 2(b)] allow us to discriminate between energy-split S- and A-type DDCs.

The SSH properties of the first-order TI give rise to topological states at the xy surfaces, whose chiral origin is characterized by the out-of-plane winding number defined as [37–39],

$$\mathcal{W}_{\perp} = \sum_{j=1}^{6} \mathcal{W}_z, \quad \mathcal{W}_z = \frac{1}{2\pi i} \oint \partial_{q_z} \ln(g_x - i g_y) d_{q_z}. \quad (3)$$

$\mathcal{W}_z$ that is the winding number of $\mathcal{H}_z$, is computed as a function of γ/γ' as shown in Fig. 3(a) (green line) and clearly displays a topological phase transition around $\gamma = \gamma'$. These topologically distinct phases are further manifested through winding contours of $g(q_z)$ at the origin when $\gamma/\gamma' < 1$ (red circle) and beyond when $\gamma/\gamma' > 1$ (blue circle) [Fig. 3(a)]. Now, we compute the projected surface dispersion of a truncated honeycomb first order TI with ten layers stacked along the z direction, see Supplemental Material [36]. We distinguish between two cases, in that Fig. 3(b) represents a $\gamma/\gamma' < 1$ interlayer coupling, whereas Fig. 3(c) is computed with $\gamma/\gamma' > 1$. The data with circles are obtained by means of numerical computations (gray bulk and surface states), whereas the colored solid lines correspond to the surface states theoretically obtained by solving Eq. (1). Indeed, as predicted, the six eigenfrequencies display a surface DDC around zero energy, but only for the nontrivial scenario.

The next dimension of the Dirac hierarchy exhibits a second-order TI when we lift the surface DDC through a Kekulé distortion ($\alpha \neq \beta$) as shown in Fig. 4(a), see the exact lattice in Supplemental Material [36]. Since the
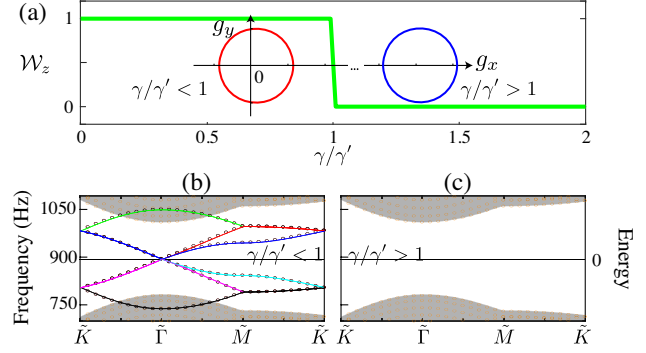

FIG. 3. First-order TI. (a) The winding $\mathcal{W}_z$ vs γ/γ'. The trajectories of $g(k)$ with different topologies for $\gamma/\gamma' < 1$ ($\gamma/\gamma' > 1$) display the presence (absence) of the winding around the origin. (b) Topological surface states appear in the xy plane when $\gamma/\gamma' < 1$, (c) while they cease to exist when $\gamma/\gamma' > 1$.

Kekulé layer maintains the chiral symmetry Γ_{xy}, the winding of $\mathcal{H}_{xy}$ along a specific hinge is defined as [40,41],

$$\mathcal{W}_{\parallel}(q_{\parallel}) = \frac{1}{2\pi i} \oint \partial_{q_{\perp}} \ln[\det \mathbf{h}(q_{\parallel}, q_{\perp})] d_{q_{\perp}}, \quad (4)$$

where $q_{\parallel}$ ($q_{\perp}$) is the normalized wave vector of $k_{\parallel}$ ($k_{\perp}$) parallel (perpendicular) to the hinge. $k_{\parallel}$ and $k_{\perp}$ are fixed through the BZ area $k_{\parallel} \times k_{\perp} = b_1 \times b_2$, where b_1, b_2 are
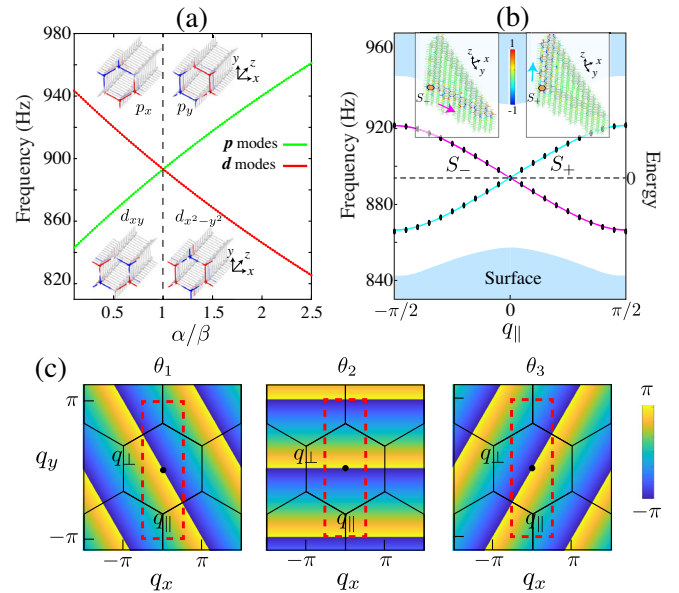

FIG. 4. Second-order TI. (a) Surface inversion diagram of the p and d states with a Z_2 topological phase transition at $\alpha = \beta$. (b) Within the gap of the projected surface states (light blue) a pair of helical hinge states (cyan and magenta, $S_{\pm}$) appears along the MZ hinges. Circles correspond to the computed results. The insets show the unidirectional propagation at 903 Hz for the clockwise S_+ and counterclockwise S_- traversing hinge states. (c) Distributions of θ_l in the 2D BZ. The red dashed box marks the integral area for the MZ hinge along $q_{\parallel}$.

the Kekulé reciprocal lattice vectors. As detailed in Supplemental Material [36], if we treat the extended cell as the combination of three sublattices, det $\boldsymbol{h}$ can be expressed entirely analytically:

$$\det \boldsymbol{h} = \rho_1 + \rho_2 + \rho_3 = |\rho|(e^{i\theta_1} + e^{i\theta_2} + e^{i\theta_3}), \quad (5)$$

where $\rho_l = (\alpha_0^3 + 2\beta_0^3)/3 - \alpha_0\beta_0^2 e^{iq_l}$ ($l = 1, 2, 3$) with $q_1 = q_x + q_y$, $q_2 = -2q_y$, $q_3 = -q_x + q_y$. θ_l is the argument of ρ_l, representing the sublattices of the Kekulé monolayer. From Eq. (5), $\mathcal{W}_{\parallel}$ is analyzed based on θ_l. The surface DDC exhibits acoustic pseudospin states [insets of Fig. 4(a)], i.e., $p_{\pm} = (p_x \pm ip_y)/\sqrt{2}$, $d_{\pm} = (d_{xy} \pm id_{x^2-y^2})/\sqrt{2}$ ($\pm$ is the spin index). Its corresponding, surface band inversion (red and green lines) takes place when spin-orbit coupling (SOC) is induced via tuning of the parameters α/β, which leads to a surface QSH phase that is captured by θ_l at the transition point. Color maps in Fig. 4(c) within the 2D BZ display discontinuous jumps among the three Kekulé phases θ_l. The Berry phase comprising these Kekulé phases read $\mathcal{B}_l(q_{\parallel}) = \frac{1}{2}\oint \partial_{q_{\perp}}\theta_l dq_{\perp}$. When the integration path $q_{\perp}$ crosses such discontinuities, the phase change is $\delta\theta = \pm 2\pi$, which allows us to determine the Berry phase $\mathcal{B}_l = \pi N_l$ through the integer N_l that counts the number of these crossings [we define the sign of N_l as positive (negative) for the $-\pi \to \pi$ ($\pi \to -\pi$) phase transitions]. Taking the molecular-zigzag (MZ) hinge along $\boldsymbol{e}_{\parallel} = (1, 0)$ as an example ($\delta = 0$), we highlight the integration path by a red dashed box in Fig. 4(c). Here, we obtain $N_1 = -1$, $N_2 = 2$, and $N_3 = -1$, which results in a total Berry phase of $\mathcal{B} = \sum \mathcal{B}_l = 0$. In fact, due to time-reversal and parity (mirror) symmetries, $\mathcal{B}$ is a Z_2 quantized number of 0 or π (mod 2π) [41], see Supplemental Material [36]. Further, $\mathcal{W}_{\parallel} = \frac{1}{\pi}\mathcal{B}$ is zero due to time-reversal invariance. However, we can define the net winding number $\mathcal{W}_n$ which accounts for the difference between positive and negative windings,

$$\mathcal{W}_n(q_{\parallel}) = \mathcal{W}_+ - \mathcal{W}_-. \quad (6)$$

Here, $\mathcal{W}_{\pm} = \sum[N_{\pm}(\text{mod } 2)]$ with $\pm$ denoting the sign of N_l. Finally, we define the in-plane winding number,

$$\mathcal{W}_I = \mathcal{W}_z \cdot \mathcal{W}_n(q_{\parallel}), \quad (7)$$

which allows to characterize the hinge and corner states, thus $\mathcal{W}_I = 2$ at the transition point $\alpha = \beta$ for the MZ hinge. Conclusively, the manifestation of these attributes is a second-order topological band gap of the surface DDC ($\alpha > \beta$), inside which a pair of helical hinge states is created. The MZ hinge dispersion is shown in Fig. 4(b) for a truncated 3D honeycomb lattice where we chose $\alpha = 0.16$, $\beta = 0.09$ and $\gamma = 0.09$, $\gamma' = 0.64$. Within the surface gap (light blue), a pair of helical hinge states $S_{\pm}$

[cyan and magenta (circles) represent theoretical (numerical) results] emerge as identified by $\mathcal{W}_I = 2$. The handedness of the hinge states creeping around its topological enclosure is showcased in the insets of Fig. 4(b), where at 903 Hz we selectively excite the respective pseudospin state to enable hinge waves propagating either clockwise (S_+) or counterclockwise (S_-). Note that, although $\mathcal{W}_I$ predicts the number of hinge states, the existence of zero energy states ($\varepsilon_{xy} = 0$) requires additional symmetry protection. Because of the MZ hinge ($\delta = 0$) exhibiting a mirror that commutes with Γ_{xy}, the hinge states degenerate at the BZ center at $\varepsilon_{xy} = 0$, forming a twofold hinge DC. It should also be mentioned that the winding $\mathcal{W}_n$ in this work is a global property defined by chiral symmetry, thus we can precisely predict the appearance of hinge states across the whole BZ. This is distinct from most of the existing works of C_6 protection where the topological phase of the DDC is guaranteed only at the symmetry point.

The last nested element of the Dirac hierarchy is unraveled by designing the third-order topological band gap. This can be achieved simply by removing the mirror from the MZ hinge such that the hinge DC at $\varepsilon_{xy} = 0$ is gapped due to the lack of mirror protection. The mirror is broken by superimposing $-\delta$ to the bonds in the y direction and $+\delta/2$ to the remaining ones as depicted in Fig. 1(d) [see also Fig. S5(a)]. The band diagram of the modified MZ hinge in a semi-periodic third-order insulator is depicted in Fig. 5(a) in which we clearly see a complete gap inhibiting surface and hinge waves to traverse with respect to their spectral color zones. Interestingly, if we ensure mirror protection at the MZ corner (it must commute with Γ_{xy}), $\mathcal{W}_I = 2$ implies a pair of midgap corner states. The corresponding finite-size computations [see Fig. S5(b)] consist of seven vertically stacked monolayer-rhombi with 34 unit cells in each layer. The various topologically confined states of this finite 3D lattice are computed and
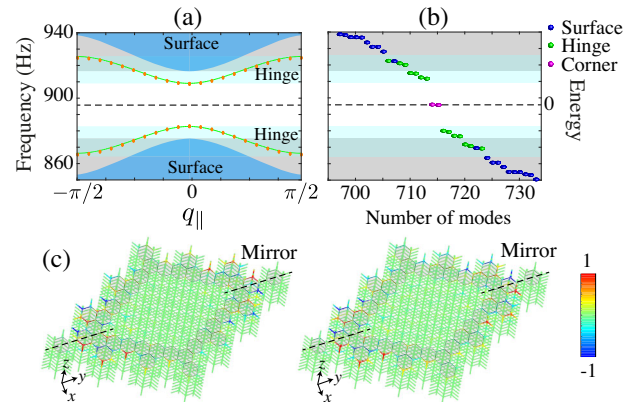

FIG. 5. Third-order TI. (a) Computed band diagram showing the gapped surface and hinge bands (circles represent numerical simulations) and (b) the corresponding eigenstates for a finite 3D lattice at their various localizations. (c) The eigenfields of the mirror-protected corner states seen in (b).

displayed in Fig. 5(b). Each spectral zone hosts eigenstates with respect to their dimensionality, i.e., our computations predict 2D surface states at around 930 Hz, 1D hinge states at 910 Hz, and 0D corner states, midgap at 895 Hz. The latter are two $\varepsilon_{xy} = 0$ corner states whose eigenfields that are displayed in Fig. 5(c) display the typical high concentration of sound at the mirror-protected corners of the 3D body.

In this work, we have demonstrated a Dirac hierarchy encompassing multiple degenerate Dirac cones, which when appropriately gapped, gives access to various topologically confined acoustic excitations comprising surface, hinge, and corner states, all using the same base configuration. Through theoretical predictions that are in good agreement with numerical simulations, we exemplify how these Dirac degeneracies and topological states of differing dimensionalities can be generated in a 3D honeycomb lattice by appropriately tuning the interlayer and intralayer coupling strengths. We foresee that this facile configuration can be readily implemented through 3D printing [42].

---

[*]lzheng@inst.uc3m.es

[†]johan.christensen@uc3m.es

[1] M. Z. Hasan and C. L. Kane, Rev. Mod. Phys. **82,** 3045 (2010).

[2] X.-L. Qi and S.-C. Zhang, Phys. Today **63,** No. 1, 33 (2010).

[3] S.-Q. Shen, Natl. Sci. Rev. **1,** 49 (2014).

[4] X.-L. Qi and S.-C. Zhang, Rev. Mod. Phys. **83,** 1057 (2011).

[5] M. Z. Hasan and J. E. Moore, Annu. Rev. Condens. Matter Phys. **2,** 55 (2011).

[6] L. He, X. Kou, and K. Wang, Phys. Status Solidi-Rapid Res. Lett. **7,** 50 (2013).

[7] P. Liu, J. Williams, and J. Cha, Nat. Rev. Mater. **4,** 479 (2019).

[8] T. Zhang, Y. Jiang, Z. Song, H. Huang, Y. He, Z. Fang, H. Weng, and C. Fang, Nature (London) **566,** 475 (2019).

[9] S. Cummer, J. Christensen, and A. Alù, Nat. Rev. Mater. **1,** 16001 (2016).

[10] X. Zhang, M. Xiao, Y. Cheng, M. Lu, and J. Christensen, Commun. Phys. **1,** 97 (2018).

[11] Z. Yang, F. Gao, X. Shi, X. Lin, Z. Gao, Y. Chong, and B. Zhang, Phys. Rev. Lett. **114,** 114301 (2015).

[12] C. He, X. Ni, H. Ge, X.-C. Sun, Y.-B. Chen, M.-H. Lu, X.-P. Liu, and Y.-F. Chen, Nat. Phys. **12,** 1124 (2016).

[13] Z. Zhang, Q. Wei, Y. Cheng, T. Zhang, D. Wu, and X. Liu, Phys. Rev. Lett. **118,** 084303 (2017).

[14] Y. Deng, H. Ge, Y. Tian, M. Lu, and Y. Jing, Phys. Rev. B **96,** 184305 (2017).

[15] Z. Zhang, Y. Tian, Y. Cheng, X. Liu, and J. Christensen, Phys. Rev. B **96,** 241306(R) (2017).

[16] Z. Zhang, Y. Tian, Y. Cheng, Q. Wei, X. Liu, and J. Christensen, Phys. Rev. Applied **9,** 034032 (2018).

[17] Z. Zhang, Y. Tian, Y. Wang, S. Gao, Y. Cheng, X. Liu, and J. Christensen, Adv. Mater. **30,** 1803229 (2018).

[18] F. Zangeneh-Nejad and R. Fleury, Phys. Rev. Lett. **122,** 014301 (2019).

[19] L.-Y. Zheng, V. Achilleos, O. Richoux, G. Theocharis, and V. Pagneux, Phys. Rev. Applied **12,** 034014 (2019).

[20] R. Chaunsali, E. Kim, A. Thakkar, P. G. Kevrekidis, and J. Yang, Phys. Rev. Lett. **119,** 024301 (2017).

[21] M. Miniaci, R. K. Pal, B. Morvan, and M. Ruzzene, Phys. Rev. X **8,** 031074 (2018).

[22] Y. Chen, X. Liu, and G. Hu, J. Mech. Phys. Solids **122,** 54 (2019).

[23] S.-Y. Huo, J.-J. Chen, H.-B. Huang, Y.-J. Wei, Z.-H. Tan, L.-Y. Feng, and X.-P. Xie, Mech. Systems Signal Process. **154,** 107543 (2021).

[24] M. Miniaci, R. K. Pal, R. Manna, and M. Ruzzene, Phys. Rev. B **100,** 024304 (2019).

[25] W. Wang, B. Bonello, B. Djafari-Rouhani, and Y. Pennec, Phys. Rev. B **100,** 140101(R) (2019).

[26] W. A. Benalcazar, B. A. Bernevig, and T. L. Hughes, Science **357,** 61 (2017).

[27] M. Serra-Garcia, V. Peri, R. Süsstrunk, O. R. Bilal, T. Larsen, L. G. Villanueva, and S. D. Huber, Nature (London) **555,** 342 (2018).

[28] Z. Zhang, B. Hu, F. Liu, Y. Cheng, X. Liu, and J. Christensen, Phys. Rev. B **101,** 220102(R) (2020).

[29] H. Fan, B. Xia, L. Tong, S. Zheng, and D. Yu, Phys. Rev. Lett. **122,** 204301 (2019).

[30] M. Ezawa, Phys. Rev. B **98,** 045125 (2018).

[31] M. Ezawa, Phys. Rev. Lett. **120,** 026801 (2018).

[32] H. Xue, Y. Yang, G. Liu, F. Gao, Y. Chong, and B. Zhang, Phys. Rev. Lett. **122,** 244301 (2019).

[33] M. Weiner, X. Ni, M. Li, A. Alù, and A. B. Khanikaev, Sci. Adv. **6,** eaay4166 (2020).

[34] X. Zhang, B.-Y. Xie, H.-F. Wang, X. Xu, Y. Tian, J.-H. Jiang, M.-H. Lu, and Y.-F. Chen, Nat. Commun. **10,** 5331 (2019).

[35] Y. Qi, C. Qiu, M. Xiao, H. He, M. Ke, and Z. Liu, Phys. Rev. Lett. **124,** 206601 (2020).

[36] See Supplemental Material at http://link.aps.org/supplemental/10.1103/PhysRevLett.127.156401 for the theoretical details, symmetry discussion, and derivation of the winding numbers.

[37] A. P. Schnyder, S. Ryu, and A. W. W. Ludwig, Phys. Rev. Lett. **102,** 196804 (2009).

[38] I. Mondragon-Shem, T. L. Hughes, J. Song, and E. Prodan, Phys. Rev. Lett. **113,** 046802 (2014).

[39] M. Maffei, A. Dauphin, F. Cardano, M. Lewenstein, and P. Massignan, New J. Phys. **20,** 013023 (2018).

[40] P. Delplace, D. Ullmo, and G. Montambaux, Phys. Rev. B **84,** 195452 (2011).

[41] T. Kariyado and Y. Hatsugai, Phys. Rev. B **88,** 245126 (2013).

[42] L.-Y. Zheng, X.-J. Zhang, M.-H. Lu, Y.-F. Chen, and J. Christensen, Mater. Today Phys. **16,** 100299 (2021).